Metal-Organic Framework Nanosheets for Thin-Film Composite Membranes with Enhanced Permeability and Selectivity

Yue Wen[†], Xingran Zhang[†], Xuesong Li[†], Zhiwei Wang*[, †], Chuyang Y. Tang[‡]

[†] State Key Laboratory of Pollution Control and Resource Reuse, Shanghai Institute of Pollution Control and Ecological Security, School of Environmental Science and Engineering, Tongji University, 1239 Siping Road, Shanghai 200092, China

[‡] Department of Civil Engineering, the University of Hong Kong, Pokfulam Road, Hong Kong S.A.R., China

Revised Manuscript Submitted to: *ACS Applied Nano Materials*

Aug, 2020 (Clean version)

ABSTRACT

Wide-spread applications of reverse osmosis (RO)-based processes call for high-performance thin-film composite (TFC) membranes. In this study, a TFC membrane by incorporating an ultrathin 2D metal-organic frameworks (MOFs) (ZnTCPP) interlayer was developed for water purification, and the mechanisms in enhancing membrane permeability and selectivity were revealed. The introduction of 2D MOF nanosheets interlayer nearly tripled the membrane water permeance (4.82±0.55 $L \cdot m^{-2} \cdot h^{-1} \cdot bar^{-1}$) with a simultaneous increase of NaCl rejection (97.4±0.6%) compared to the control, successfully overcoming the permeability-selectivity trade-off. Combined use of quartz crystal microbalance and transmission electron microscopy revealed that the MOF interlayer induced the significant changes in the polyamide membrane structure that favors water permeation, *i.e.*, decreased intrinsic thickness, increased void volume fraction, and enhanced effective filtration surface area. Such improvements in the polyamide structure can be attributed to the synergistic effects of enhanced confinement to interfacially degassed nanobubbles and reduced diffusivity of *m*-phenylenediamine monomers due to the MOF interlayer. This interlayer also increased the cross-linking degree of polyamide layer (contributing to the increase of membrane selectivity) and served as a gutter layer (to further enhance membrane permeance by reducing the geometric restriction of the support layer). Our study highlights the potential of using ultrathin MOF nanosheets to fabricate high-performance TFC membranes for desalination and water purification.

KEYWORDS: *Thin-film composite membrane, 2D metal-organic framework nanosheets, interfacial polymerization, water purification, wastewater treatment*

INTRODUCTION

Reverse osmosis (RO) membrane-based processes have been extensively used for desalination and water purification in addressing the critical challenge of water scarcity.[1, 2] Polyamide (PA) thin-film composite (TFC) membranes are the dominant membranes for RO applications due to their high separation performance,[3, 4] which are fabricated via interfacial polymerization (IP) using an amine monomer, *e.g.*, *m*-phenylenediamine (MPD), and an acyl chloride monomer, *e.g.*, trimesoyl chloride (TMC), on a porous support.[5, 6] The interfacial polymerization leads to a highly selective polyamide layer with an apparent thickness of 50-300 nm and a typical "ridge and valley" surface morphology.[7, 8] This thin polyamide layer plays a key role in governing the water permeability and salt rejection of the TFC membrane.

However, the separation performance of commercial TFC membranes is constrained by an upper bound, *i.e.*, trade-off between water permeability and selectivity,[9, 10] which is dependent on the intrinsic properties of polyamide layer.[11-14] Decrease of the intrinsic thickness of the polyamide layer increases membrane permeability,[14, 15] and increase of effective surface area (*e.g.*, Turing structure surface and more crumpled 'ridge and valley' morphology) also leads to the improvement of water-salt separation performance.[5, 16] Therefore, it is of great importance to fabricate ultrathin TFC membranes with large effective surface area and low intrinsic thickness to overcome the long-standing permeability-selectivity trade-off.

An alternative way to break the trade-off is to fabricate thin-film nanocomposite (TFN) membranes, providing preferential water flow paths for permeance while maintaining high solute rejection.[17] Nanofillers involving nanoparticles and metal organic frameworks (MOFs) (UiO-66,[18, 19] ZIF-8,[20, 21] and HKUST-1[22]) have been incorporated into the polyamide layer to increase water permeability. However, selectivity may be compromised due to possible defects between MOF

nanoparticles and polyamide membrane although water permeability is enhanced. These inherent drawbacks prompt us to explore a more efficient approach to fabricate a highly permeable and selective TFC membrane through a precise manipulation of the structure of the polyamide film.

In this work, we use MOF nanosheets as an interlayer rather than nanofiller to prepare a high-performance TFC membrane. Two-dimensional MOF nanosheets are highly attractive because of their high-aspect-ratio nanostructure and ideally (sub)nanometer thickness,[23] exhibiting high potential to fabricate ultra-permeable materials. A number of nanomaterials such as $Cd(OH)_2$ nanostrands[15], carbon nanotubes[24, 25], graphene oxide (GO),[26] and tannic acid/Fe^{3+} [27] have been employed to construct the interlayer for the fabrication of TFC membranes. Most studies used hydrophilic interlayer to create thin and smooth polyamide layers for nanofiltration membrane. [25, 28-30] Decreasing the surface pore size was also effective to create rougher PA layers of FO membrane because of the intensified IP reaction.[31] Compared to those nanomaterials, 2D MOF nanosheets not only offer a hydrophilic surface for the polyamide formation, but also exhibit high density and regular distribution of selective pores in the MOF nanosheets, which leads to decreased water transport resistance.[32] Besides, MOF nanosheets show greater potential to be used as an interlayer for fabricating high-performance TFC membranes, which was attributed to their high tunability in pore structure and surface functionality.[33] We hypothesize that highly porous MOF nanosheets may act as a reservoir for aqueous solution and control the release of MPD monomers, which is beneficial for forming polyamide membrane with reduced intrinsic thickness. Recent literature also highlight the critical role of degassing of CO_2 nanobubbles during IP reaction and their confinement by the support membrane in shaping the structure and surface morphology of polyamide.[5, 34] Inspired by these recent findings, we further hypothesize that the MOF interlayer

can enhance the 'ridge and valley' morphology and increase the effective surface area by providing improved confinement effect.

Based on these hypotheses, we used highly-porous MOF nanosheets (zinc(II) tetrakis(4-carboxy-phenyl)porphyrin) (ZnTCPP) with high flexibility and hydrophilicity[35, 36]) as an interlayer, which could serve as a hydrophilic and dense layer with uniform fine pores for the interfacial polymerization of the polyamide rejection layer. The as-prepared polyamide membrane showed a simultaneous increase of permeability and selectivity, successfully breaking the permeability-selectivity trade-off. The mechanisms of 2D MOF nanosheets in enhancing membrane's selectivity and permeability were further elucidated. Our study provides a new direction, incorporating ultrathin MOF nanosheet interlayer, to fabricate high-performance TFC membranes for desalination and water purification.

MATERIALS AND METHODS

Chemicals. Ultrafiltration poly(ether sulfone) (PES) membranes (20 kDa, GC-UF0202, Microdyn-Nadir Inc., Wiesbaden, GM) were used as the support layer for TFC membrane fabrication. MPD and TMC were used for interfacial polymerization of polyamide (Sigma−Aldrich, St. Louis, MO). *n*-Hexane was used to dissolve TMC (Sigma−Aldrich). $Zn(NO_3)_2 \cdot 6H_2O$, polyvinylpyrrolidone (PVP), tetrakis(4-carboxyphenyl)porphyrin (TCPP) and pyrazine were used to synthesize Zn-TCPP, which were all purchased from Sigma−Aldrich. N,N-dimethyllformamide (DMF) and ethanol were received from Sigma−Aldrich. Toluidine blue O (TBO) (Sigma−Aldrich) was used to determine the membrane surface carboxyl group density. Other chemicals including NaCl, CH_2Cl_2, polyethylene glycol (PEG), dimethylacetamide (DMAc)

and isopropanol were purchased from Aladdin (China). Deionized (DI) water was used throughout all experiments.

Preparation of MOFs. Zn-TCPP nanosheets were synthesized according to the modified surfactant-assisted method.[37] Briefly, $Zn(NO_3)_2 \cdot 6H_2O$ (45 mg, 0.15 mmol), PVP (200 mg) and pyrazine (8 mg) were dissolved in 120 mL of the mixture of DMF and ethanol (v:v=3:1). TCPP (40 mg, 0.05 mmol) dissolved in 40 mL of the mixture of DMF and ethanol (v:v=3:1) was dropwise added into the aforementioned solution. The mixed solution was sonicated for 10 min and then placed in an oven at 80°C for 20 h. The resultant purple nanosheets were centrifuged followed by washing thoroughly with ethanol. The pristine nanosheets were acquired through a thorough washing with CH_2Cl_2 via Soxhlet extraction for one day to remove PVP and DMF, followed by centrifugation and drying under a reduced pressure.

Preparation of TFC Membranes. The fabrication process of the modified PES-MOF membrane and TFC-MOF membrane is shown in Figure 1. To construct a MOF interlayer, 9.0 mg of Zn-TCPP nanosheets were dispersed in 600 mL ethanol by sonication, and a certain volume of Zn-TCPP suspension (0 mL, 12 mL, 24 mL and 48 mL) was filtrated through a PES support layer with an effective area of 13.4 cm^2 under 4.0 bar. The resultant support layers were denoted as PES-MOF-0, PES-MOF-1, PES-MOF-2, and PES-MOF-3, respectively.

For interfacial polymerization, the support was first soaked in 2.0 wt% MPD solution for 2 min. The excess MPD solution on the support surface was then removed by nitrogen gas using an air-knife. Next, the MPD-saturated membrane was reacted with 0.1 wt% TMC in a hexane solution for 45 s. After rinsing with hexane, the membrane was cured at 70°C for 5 min. The membranes fabricated on PES-MOF-0, PES-MOF-1, PES-MOF-2, and PES-MOF-3 membranes were denoted

as TFC-MOF-0, TFC-MOF-1, TFC-MOF-2 and TFC-MOF-3, respectively. All fabricated TFC membranes were stored in DI water at 4°C for further characterization and tests.

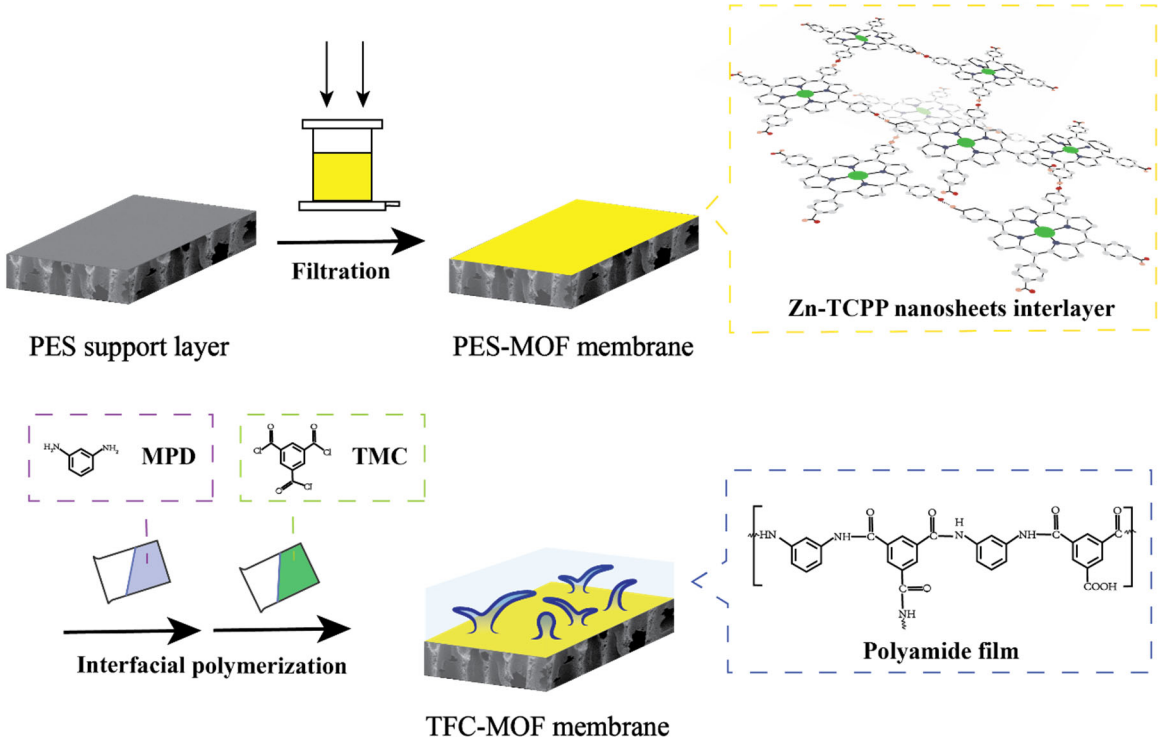

Figure 1. Fabrication process of PES-MOF membrane and TFC-MOF membrane.

A TFC membrane was also prepared by fabricating a polyamide film at a free aqueous-organic interface and then transferred onto a support.[38] In brief, the support membrane (PES-MOF-0, PES-MOF-1, PES-MOF-2, or PES-MOF-3) was placed in a glass container and was fully immersed in the MPD aqueous solution (2.0 wt% MPD). The MPD solution level was 3 cm above the support membrane surface to ensure the formation of polyamide film at a free interface instead of directly on the support membrane. Then 0.1% TMC-hexane solution was carefully poured onto the surface of MPD solution. A similar free interface was created between MPD aqueous solution and TMC hexane solution in the glass containers regardless of the type of support membrane. The stopcock of the container (located at the bottom) was then opened to drain the solution until the polyamide

film gently landed on the support. The total reaction time for interfacial polymerization was 1 min. The resulting membranes were rinsed with excess hexane, followed by curing at 70°C for 5 min to reinforce the interfacial adhesion between the polyamide nanofilm and the support.[7, 38] The resultant membranes were stored in DI water at 4°C, which were denoted as FR-0, FR-1, FR-2, and FR-3, respectively.

Characterization of Membranes. Characterization methods for MOF nanosheets are documented in SI Section S1, with the properties of MOF nanosheets shown in SI Section S2. Field emission scanning electron microscope (FESEM, SU8010, Hitachi, Japan) was used to observe the surface and cross-section morphologies. The chemical structure on the support layer was characterized using X-ray diffraction (XRD, Brucker D8, Bruker Corporation, USA), X-ray photoelectron spectroscopy (XPS, AXIS UltraDLD, Kratos Analytical Ltd., U.K.) and attenuated total reflectance-Fourier transform infrared spectroscopy (ATR-FTIR, Nicolet 6700, Thermo Electron Corporation, USA).[39] Surface roughness of MOF interlayers was measured by an atomic force microscopy (AFM, Veeco NanoScope MultiMode IIIa, USA). Sessile drop contact angle measurement was used to determine the surface hydrophilicity using an OCA 15 Plus instrument (Data Physics GmbH, Germany) at ambient temperature. The surface zeta potential of the TFC membrane was measured at pH 7.0 using a streaming potential analyzer (SurPASS3, Anton Paar, Austria) with 0.01 M KCl solution as a background electrolyte.[40] The pure water flux of the support layer was tested using a stirred ultrafiltration cell (UFSC05001, Millipore, US) at 4 bar. The molecular weight cut-off (MWCO) was measured using solute transport method and calculated via various molecular weight of PEG (see details in SI Section S5).[41, 42] The concentration of PEG was measured by a total organic carbon analyzer (TOC-L CPH, Shimadzu, Japan).

The functional groups, elemental compositions, surface roughness, contact angle (CA), and zeta potential of the polyamide film were characterized using ATR-FTIR, XPS, AFM, sessile drop CA, and zeta potential analysis, respectively. The TBO technique was used to measure the surface carboxyl groups density of the TFC membrane.[43] Surface and cross-section morphologies of the TFC membrane were visualized by FESEM (S-4800 & JEOL JSM-7800F Prime, Hitachi & JEOL, Japan). The apparent thickness (δ_{app}) of the polyamide film was obtained by measuring the average vertical distance between the frontside and the bottom of the polyamide film (*i.e.*, the thickness of the whole polyamide layer). The intrinsic thickness (δ_{int}) was acquired by measuring the average nodular/leaf wall thickness, which represents the exact thickness of the key barrier layer that controls the water permeance. The measurement is illustrated in SI Figure S5 using TEM (TALOS F200X, Thermofisher Scientific, U.S.). The void volume fraction (*f*) of polyamide layers was calculated using Eq. (1):

$$f(\%) = \frac{\text{Pore volume}}{\text{Active layer volume} + \text{Pore volume}} \times 100\% \quad (1)$$

where the active layer and pore volume were measured by ImageJ software to calculate the accumulated pixels in active layer and in pores within active layer, respectively (see details in SI Figure S8).

Measurement of diffusivity of MPD monomers from PES-MOF-0, PES-MOF-1, PES-MOF-2, and PES-MOF-3 support membranes during interfacial polymerization is described in SI Section S12. In brief, the MPD-saturated support membranes were immersed into DI water for predetermined time intervals to allow a diffusion of MPD into water. The aqueous solution was then collected to measure the MPD concentration using reversed phase high-performance liquid chromatography (HPLC, Agilent 1200).[44]

Water permeance and salt rejection of the TFC membranes and support-free TFC membranes were evaluated by a laboratory-scale cross-flow filtration system at 16.0 bar and 24 ± 0.1°C as described in our previous study.[45] The membranes each with an effective area (A_m) of 6.25 cm^2 were pre-compacted with DI water at a crossflow rate of 22.4 cm/s for 2 h to achieve a stable flux before measurement. Salt rejection was tested with 2000 mg/L NaCl feed solution. The water flux was calculated by Eq. (2):

$$J_W = \frac{\Delta V}{A_m \cdot \Delta t} \quad (2)$$

where J_w represents permeate flux ($L \cdot m^{-2} \cdot h^{-1}$) and ΔV is the volume of the permeated solution (L) collected during a certain period of time Δt (h).

The salt rejection was calculated according to Eq. (3):

$$R = \left(1 - \frac{C_p}{C_f}\right) \times 100\% \quad (3)$$

where C_f (mg/L) and C_p (mg/L) are the concentrations of NaCl in the feed and permeate, respectively. The salt concentration was determined by measuring the conductivity of solution using an electrical conductivity meter (Cole-Parmer, USA).

To evaluate the stability of the RO membranes, TFC membranes were soaked in water for 15 d. The separation performance of TFC membranes after soaking was evaluated in a cross-flow filtration system.

Measurement of Intrinsic Structural Change in Active Layer of TFC Membranes Using Quartz Crystal Microbalance (QCM). QCM analysis (Q-sense E4, Biolin Scientific, Sweden) was used to investigate the structural changes in active layers resulting from different IP reaction process on PES support layer and MOF nanosheets interlayers. The polyamide films were isolated

from TFC-MOF-0, TFC-MOF-1, TFC-MOF-2, and TFC-MOF-3 membranes and mounted onto QCM sensors (QSX301, Qsense) as described in detail elsewhere.[46] It has been verified that the isolation approach can maintain the original structures of the active layers.[14, 47] The MOF interlayers were thoroughly removed by DMAc and examined by inductively coupled plasma mass spectrometry (ICP-MS Agilent 7700, Agilent Technologies Inc., USA) before the experiments, [48] ensuring that only the polyamide active layers were coated on QCM sensors. The areal mass of active layers (m_{AL}^{0}, ng/cm^2) and the areal mass of water absorbed by active layers ($m_{\mathrm{AL}}^{\mathrm{w}}$, ng/cm^2) when exposed to liquid water were measured by a Q-sense flow module (QFM401, Biolin Scientific, MD). The m_{AL}^{0} was obtained from the difference in QCM response between the coated and corresponding uncoated sensors when being exposed to dry nitrogen gas. The $m_{\mathrm{AL}}^{\mathrm{w}}$ was obtained from the difference in QCM response for the coated sensor between exposure to ultrapure water and to dry nitrogen. During the measurement, the water flow rate was 0.14 mL/min and the sensor response was monitored until the system reached equilibrium (typically 10 min).[49] In addition, a Q-sense humidity module (QHM401, Biolin Scientific, Lithicum Heights, MD) was used to measure the areal mass of water absorbed by active layers after exposure to nitrogen gas at 94% relative humidity ($m_{\mathrm{AL0}}^{\mathrm{w}}$, ng/cm^2). The $m_{\mathrm{AL0}}^{\mathrm{w}}$ was obtained from the difference response for the coated sensor being exposed to humidified nitrogen gas and to dry nitrogen gas at 94% RH. The $m_{\mathrm{AL0}}^{\mathrm{w}}$ measured the water uptake by the active layer polymer itself (excluding the water contained by pores), while the $m_{\mathrm{AL}}^{\mathrm{w}}$ calculated the water uptake by the whole active layer (including pores). The measurement was conducted with the water flow rate of 0.08 mL/min.[50, 51]

For each membrane, the intrinsic thickness (δ_{int}) of active layer was calculated based the measurement of m_{AL}^{0} via Eq. (4):

$$\delta_{\text{int}} = \frac{m_{\text{AL}}^{0}}{\rho_{\text{AL}} \times s_{\text{AL}} \times \text{SAR}} \quad (4)$$

where ρ_{AL} =1.24 g/cm^3 corresponds to the reported dry mass density of polyamide active layers,[52] s_{AL} represents the planar area (1.54 cm^2) of active layers, and SAR represents surface area ratio measured by TEM (%) (see details in SI Figure S8) and AFM (%), calculated as the ratio of the effective three-dimensional surface area over its projected planar area.[14, 53]

The void volume fraction (*f*) of active layers was calculated based on m_{AL}^{0}, m_{AL}^{w}, and $m_{\text{AL0}}^{\text{w}}$ according to Eq. (5):[50]

$$f(\%) = \frac{\text{Pore volume}}{\text{Active layer volume} + \text{Pore volume}} = \frac{(m_{\text{AL}}^{\text{w}} - m_{\text{AL0}}^{\text{w}})/\rho_{\text{w}}}{m_{\text{AL}}^{0}/\rho_{\text{AL}} + (m_{\text{AL}}^{\text{w}} - m_{\text{AL0}}^{\text{w}})/\rho_{\text{w}}} \times 100\% \quad (5)$$

where ρ_{w} =1.0 g/cm^3 corresponds to water density.

RESULTS AND DISCUSSION

Preparation and Characterization of MOF Nanosheet Interlayer. XPS analysis show the presence of Zn, a characteristic element of Zn-TCPP, on the support surface (SI Table S2). The Zn elemental ratio increased with greater filtrated volume of the MOF suspension, demonstrating a successful coating of MOF interlayer onto the support. ATR-FITR results also show that the modified support had the characteristic C=O stretching vibration, owing to the coating of MOF nanosheets (Figure 2a). A characteristic sharp peak at 7.5º in the XRD spectra for MOF coated membrane represents the (002) crystallographic plane of the laminar MOF structure, suggesting that the MOFs were stacked in an ordered manner (Figure 2b). The nanosheets with preferential orientation led to the exposure of their pores in the direction of water flux,[36] enabling the formation of a permeable MOF nanosheet layer. SEM images (Figure 3) showed that continuous and

relatively smooth laminate layers were formed on the PES support layers of PES-MOF-1, PES-MOF-2 and PES-MOF-3 membranes, which was further confirmed by AFM analysis. AFM analysis reveal that the roughness of the support slightly increased with greater filtrated volume of the MOF suspension (Figure 2c). Nevertheless, the root mean square roughness (R_q) of all the supports remained below 25 nm, ensuring a relatively smooth surface for the subsequent interfacial polymerization.[54] As shown in Figure 2d and SI Figure S3, the deposition of MOF nanosheets led to an increase of surface hydrophilicity and an increase of surface negative charge, which could be attributed to the presence of carboxylic acid groups on MOFs.[37, 55] As summarized in Table 1, with the MOF volume increasing from 0 mL to 24 mL, the thickness of interlayers increased from 0 nm to 66±10 nm (SI Figure S4), and MWCO of supports decreased from 46,000 Da to 23,000 Da, suggesting that the MOF coating effectively reduced the pore size of the support (see SI Table S1). The cross-sectional images are shown in SI Figure S4. For all the MOF coated PES membranes (SI Figure S4b~d), the nanosheets formed an obvious continuous laminate layer. These results confirmed the formation of an ultrathin, compact, and highly ordered laminate MOF interlayer on the PES support. After further increase of MOF volume to 48 mL, the MWCO slightly increased, which might be attributed to some tiny crumples and hump-like protuberances shown on PES-MOF-3 membrane (Figure 3d).[56]

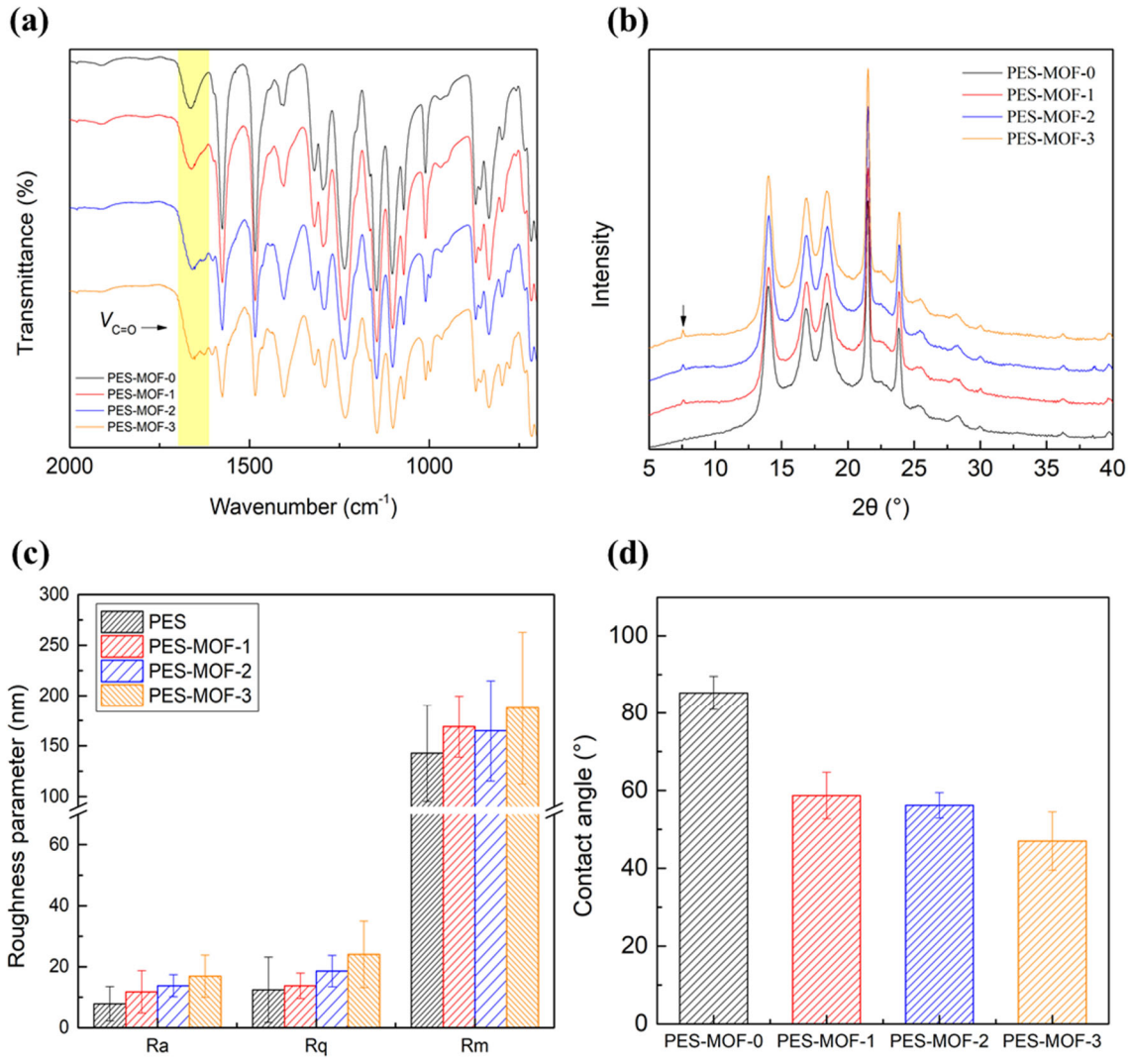

Figure 2. Characterization of MOF interlayers. (a) FTIR spectra, (b) XRD pattern, (c) surface roughness (n = 3), and (d) contact angle (n = 6).

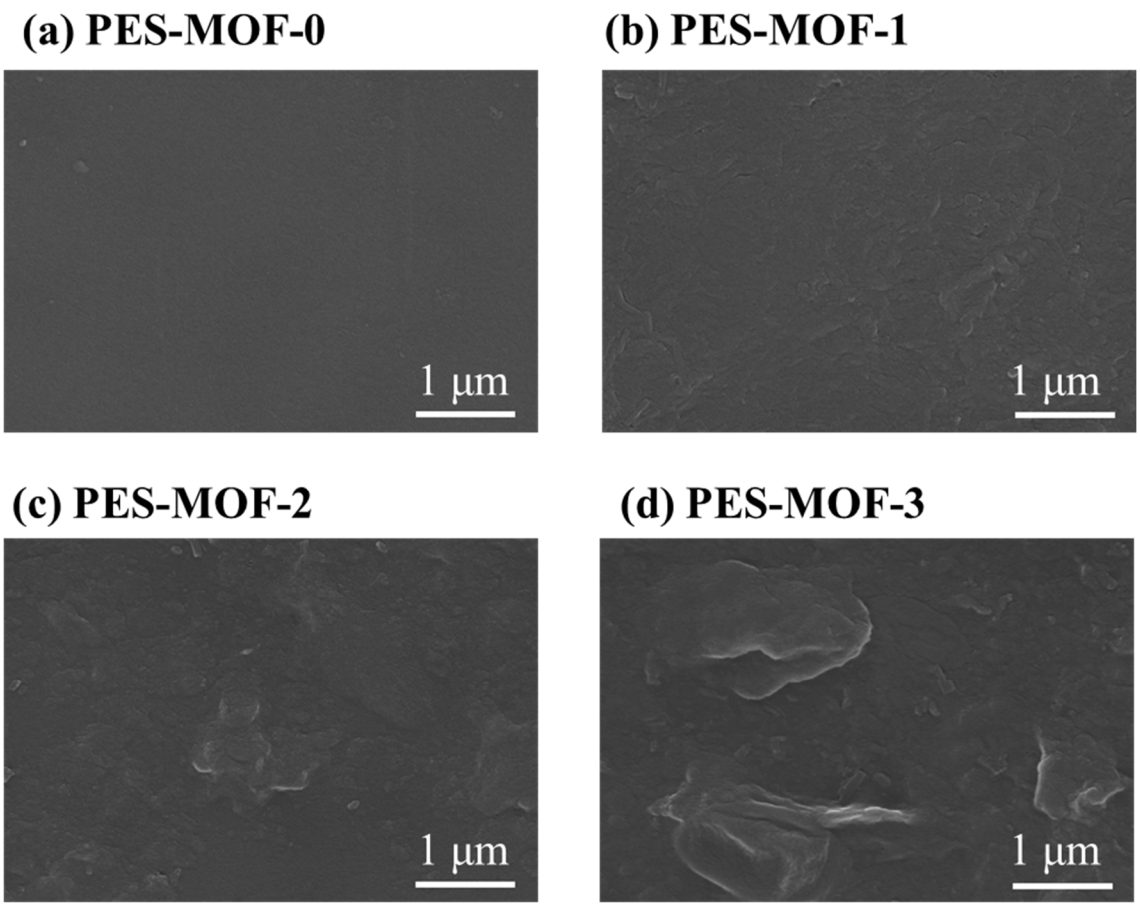

Figure 3. Surface SEM images of (a) PES-MOF-0, (b) PES-MOF-1, (c) PES-MOF-2, and (d) PES-MOF-3 membranes.

Table 1. Structure parameter of the pristine PES membrane and the PES-MOF membrane substrate.

Membranes	**MOF dispersion volume (mL)**	**MWCO (kDa)**	**Thickness of MOF layer (nm)**

PES-MOF-0	0	46	/
PES-MOF-1	12	31	36±6
PES-MOF-2	24	18	66±10
PES-MOF-3	48	23	166±26

Impacts of MOF Interlayer on Polyamide Formation of TFC Membranes. Figure 4 shows the surface and cross-section morphologies of TFC membranes fabricated on the pristine and MOF-modified supports. For TFC-MOF-0, a typical "ridge-and-valley" structure with nodular and leaf-like features was observed in the surface image. According to the recent literature, such features are created by the release of nanosized gas bubbles that are encapsulated within the polyamide layer during interfacial polymerization.[5, 57] Those gas bubbles were mainly generated in two ways: (i) the heat generation during interfacial polymerization process reduced the solubility of dissolved gases in solution; (ii) HCl generated as a byproduct during IP process accelerated the formation of CO_2.[5] The cross-sectional images of TFC-MOF-0 exhibited the features with single-layer structure consisting of discrete nodules. With the addition of MOF nanosheets interlayers, more extensive leaf-like features of larger size were observed. Especially for TFC-MOF-2 and TFC-MOF-3 membranes, these leaf-like features with few nodules dominated the membrane surface morphology. In addition, some of the larger leaves merged together, forming interconnected "belts". The cross-sectional images provided direct observation of the dual-layer structure, *i.e.*, a basal nodular layer overlaid by an additional exterior "belt" layer. Similar dual-layer structure has been recently reported for some polyamide membranes possessing higher water permeability,[14, 34] which are ascribed to the more favorable interfacial degassing conditions (*e.g.*, with the addition of sodium bicarbonate in MPD solution for enhanced degassing of CO_2 [34]).

Typically, due to the resistance to air movement of substrate layer, the formed gas nanobubbles in aqueous solution side tended to move towards the IP reaction interface and created "ridge-and-valley" structure. In the current study, the dense interlayer with smaller surface pore size could more effectively retain the degassed nanobubbles and prevent their escaping through the porous support layer, resulting in enhanced confinement by the support membrane and improved encapsulation of the gas bubbles by the polyamide layer for roughness formation.[58] These leaf-like and belt-like features were favorable to create additional filtration areas (*e.g.*, SAR measured by TEM of 848.5±83.5% for TFC-MOF-2 vs. 419.7±26.8% for TFC-MOF-0, see Figure 5a),[14, 35, 59] thus enhancing the separation performance of TFC-MOF membranes. However, SAR results measured by AFM did not match well with that by the TEM analysis (see SI Figure S9), which was mainly attributed to the inherent limitation of AFM measurement that it cannot assess the internal features of PA film.[34] As a result, the effective membrane area was greatly underestimated.

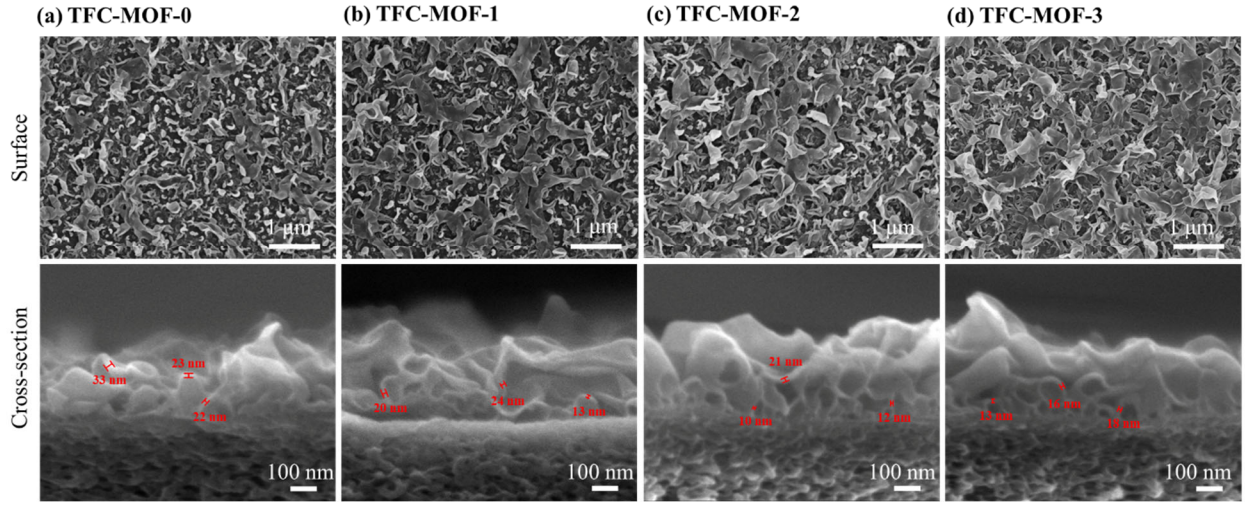

Figure 4. Surface and cross-section SEM images of (a) TFC-MOF-0 membrane, (b) TFC-MOF-1 membrane, (c) TFC-MOF-2 membrane, and (d) TFC-MOF-3 membrane.

The incorporation of MOF interlayer into TFC membrane might also affect the intrinsic thickness of the PA film (*i.e.*, the wall thickness of nodules or leaves[14, 35, 60]), whose value is a better representation of the actual thickness of the rejection layer that controls the water permeance. TEM analysis shows that the intrinsic thickness decreased from 29.0±3.6 nm (TFC-MOF-0) to 17.4±1.9 nm (TFC-MOF-3) (Figure 5b and SI Figure S6) despite their similar apparent thickness (*i.e.*, the thickness of the entire PA layer including its voids) (SI Figure S7). The intrinsic thickness of polyamide layers was mainly in the range of 10-30 nm, in good agreement with recent membrane characterization studies.[14, 35] This value is approximately an order of magnitude lower than the apparent thickness, and a thinner intrinsic thickness is beneficial for improving water permeance.[15]

QCM was further used to reveal the intrinsic thickness of the PA layer. As shown in Figure 5b, the intrinsic thickness of the TFC-MOF-2 membrane measured by QCM was decreased by approximately 4 folds compared to that of the TFC-MOF-0 membrane, while that measured by TEM only decreased by 2 folds. This difference might be attributed to the difficulty of differentiating the boundary of active layer in the TEM images once the thickness of nodule/leaf structures became too low, resulting in the poorer accuracy of the quantification. The dramatic decrease of the intrinsic thickness of TFC-MOF membranes may facilitate fast water transport through the barrier layers. Figure 5b also shows that the void volume fraction measured by QCM increased from 10.1±1.5% (TFC-MOF-0) to 37.3±7.3% (TFC-MOF-2) after the incorporation of interlayer, corresponding to a higher water uptake ability for TFC-MOF membranes (SI Figure S10) that favors water transport. These results are consistent with the improved retention of the degassed nanobubbles by the MOF-loaded support layer. However, the TFC-MOF-3 membrane exhibited an increase of intrinsic thickness and a decrease of void volume fraction compared to

TFC-MOF-2, possibly attributed to the larger pore size of the interlayer affecting the PA formation. Therefore, TFC-MOF-3 exhibited a decrease of permeance.

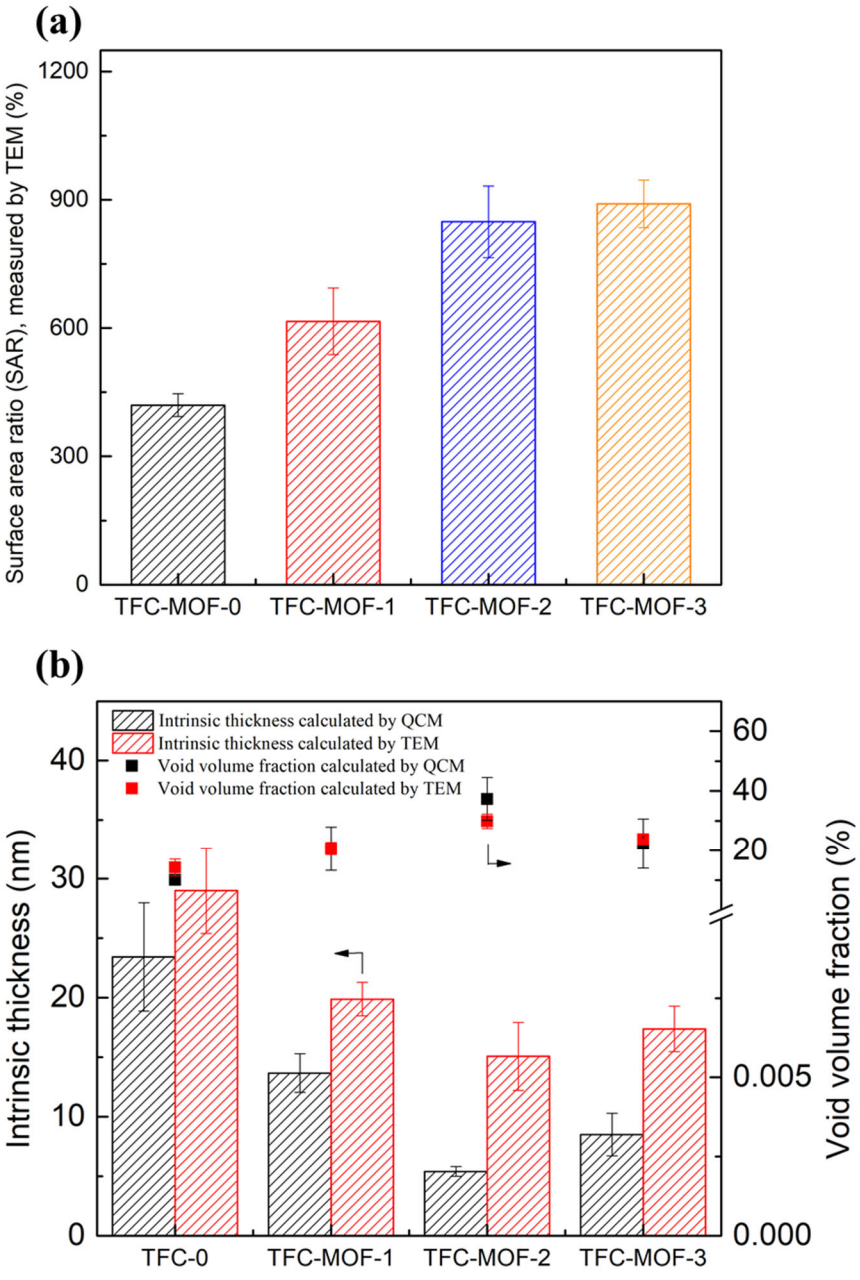

Figure 5. (a) The surface area ratio (SAR) measured by TEM analysis (n=10) and (b) the intrinsic thickness and pore void fraction of the PA layer of TFC-MOF-0, TFC-MOF-1, TFC-MOF-2, and TFC-MOF-3 membranes measured by QCM analysis (n=3) and TEM (n=10).

As shown in Figure 6a, all the membranes had similar roughness measured by AFM, suggesting that AFM failed to reveal the internal features of PA layers such as the difference between nodular and belt-like features which were observed by SEM.[34] The change of the morphology did not influence the contact angle of TFC membranes (Figure 6b). The carboxyl group density on the PA layer, as shown in Figure 6c, decreased with the increase of interlayer MOF dosage, which is in agreement with the higher cross-linking degree of membranes from XPS results (SI Table S3) and decreased negative zeta potentials (Figure 6d).[45] The high cross-linking degree might be attributed to the impeded heat dissipation/transfer by dense interlayer,[61, 62] which would accelerate the migration rate of MPD into hexane and promote the reaction between acyl chloride groups and diamine groups.[63] The higher cross-linking degree could enhance the rejection properties of the membranes. However, with the further increase of the interlayer MOF dosage, the cross-linking degree did not significantly increase, attributed to the larger pore size on the PES-MOF-3 membrane facilitating heat dissipation.

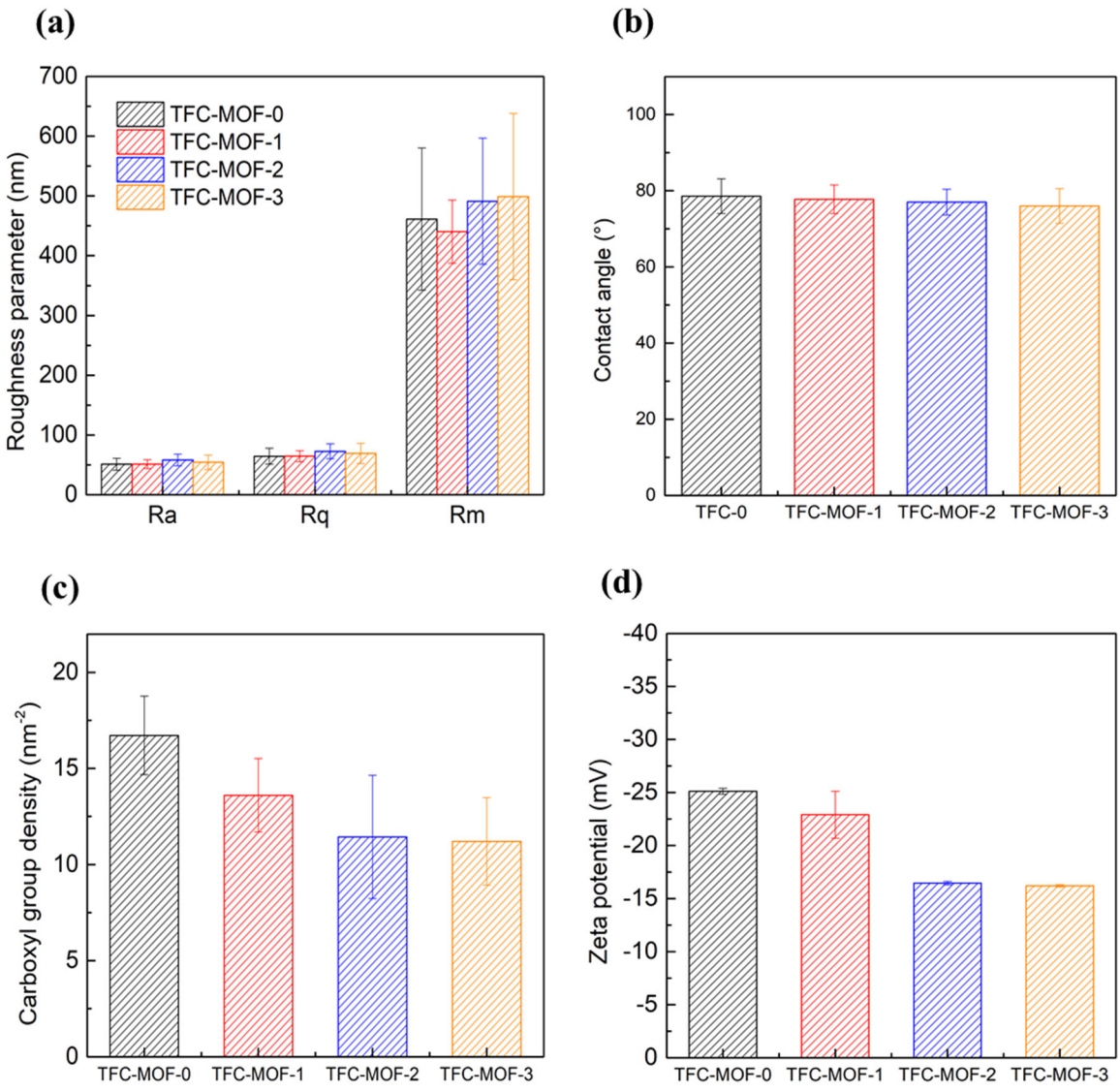

Figure 6. Characterization of TFC-MOF-0, TFC-MOF-1, TFC-MOF-2, and TFC-MOF-3 membranes. (a) surface roughness (n = 3), (b) water contact angle (n = 6), (c) carboxyl group density analysis (n = 6), and (d) zeta potential properties (n = 3).

Impacts of MOF Interlayer on Separation Performance of TFC Membranes. The separation performance of TFC membranes was investigated in an RO cross-flow filtration system. Membrane permeance was significantly enhanced with the increase of the MOF dosages (Figure

7a), ascribed to the increase of leaf-like and belt-like features (*i.e.*, greater effective filtration area) and the decrease of intrinsic thickness of PA membranes. The salt rejection also increased ($p < 0.05$ for TFC-MOF-2 and TFC-MOF-3 compared to TFC-MOF-0) because of the higher cross-linking degrees of the TFC-MOF membranes (SI Table S3). For instance, the permeance of TFC-MOF-2 membrane was dramatically improved by 282%, with the salt (NaCl) rejection rate enhanced from 95.6±1.1% (comparable with other works[19, 64-66]) to 97.4±0.6% ($p < 0.05$). Compared to commercial brackish water RO membranes with comparable permeability performance, the salt rejection of the TFC-MOF-2 membrane is obviously higher.[5, 9, 67] With the further increase of MOF dosage, the permeance of TFC-MOF-3 membrane decreased compared to TFC-MOF-1 and TFC-MOF-2, which is consistent with the increase of intrinsic thickness and decrease of void volume fraction of TFC-MOF-3 (Figure 5). The stability of MOF layers was evaluated by measuring the separation performance after soaking in water for 15 d. Results show that the separation performance did not change significantly (SI Figure S11), confirming the stability of TFC membranes.

The role of the MOF nanosheet interlayers in the permeation improvement of TFC membranes was further investigated via separation performance measurement of FR-0, FR-1, FR-2, and FR-3 membranes. Those membranes, which were made from support-free interfacial polymerization,[7, 38] had the same polyamide layers but different support layers (including PES-MOF-0, PES-MOF-1, PES-MOF-2, and PES-MOF-3 support). As shown in Figure 7b, the permeance increased with the increased MOF dosages of interlayers, while the rejection property did not change significantly among the FR membranes. This suggested that compared with the PES support without MOFs, the interlayer could act as a gutter layer, contributing to the enhanced membrane permeance by reducing the geometric restriction of the support.

It is noteworthy that compared to FR membranes, the permeance of their TFC counterparts was consistently higher. Besides, the permeance enhancement ratio of TFC-MOF-2 over TFC-MOF-0 was approximately 282%, while that of FR-2 membrane over FR-0 was only approximately 175%, suggesting that the gutter mechanism alone cannot fully explain the enhancement in permeance. As shown in SI Figure S12, the polyamide films of FR membrane were very thin and smooth, which was mainly attributed to the more rapid heat dissipation in free aqueous solution.[7] The additional enhancement of TFC membranes was due to the improved roughness formation on the substrates (by providing better confinement) compared to free interface.[58] The confinement effect has also been reported to form polyamide membranes with reduced defects,[58] which explains the generally higher rejection of TFC membranes compared to FR membranes (Figure 7).

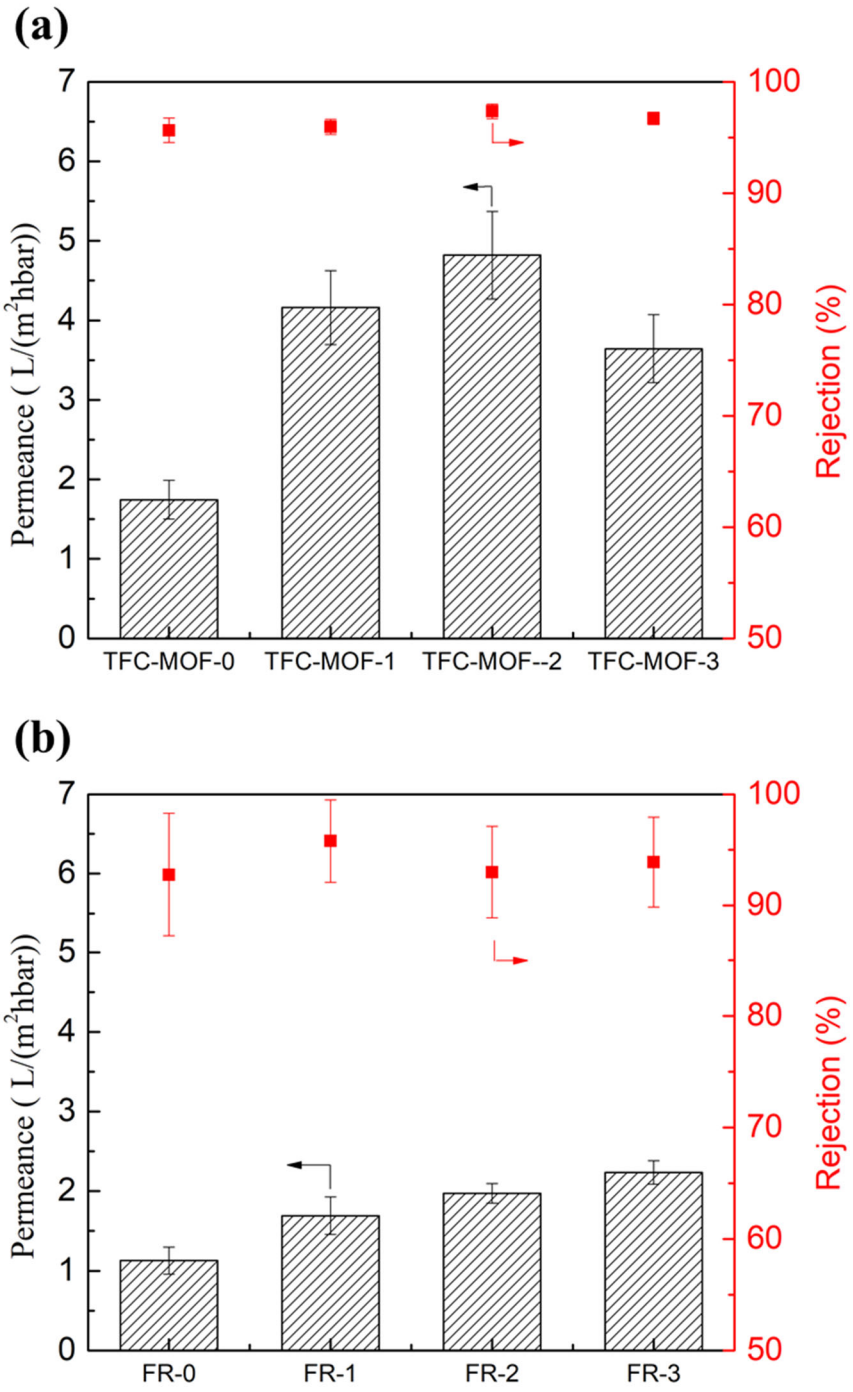

Figure 7. (a) Separation performance of TFC-MOF-0, TFC-MOF-1, TFC-MOF-2, and TFC-MOF-3 membranes (n = 6), (b) separation performance of FR-0, FR-1, FR-2, and FR-3 (with support-free PA layers landed on various supports) (n = 6).

Mechanisms of MOF Nanosheets in Enhancing Permeability and Selectivity. We demonstrate that the MOF nanosheets on the PES support play a crucial role in determining the structure and morphology of the polyamide film. As schematically illustrated in Figure 8, the confinement effect caused by the dense MOF interlayers can prevent the escape of degassed nanobubbles, resulting in larger filtration areas of polyamide membranes.[34, 58] On the other hand, the diffusivity of diamine from PES-MOF membrane was significantly decreased compared to that from pristine PES membrane (with the results shown in SI Figure S13), which can be attributed to the intrinsic hydrophilicity of the MOF interlayers and thus the increased affinity through hydrogen bond between interlayer and MPD.[68] The higher affinity downregulated the diffusivity of diamine, which could decrease the thickness of the selective layer according to the kinetic model for polyamide formation.[28, 69] With gas bubbles growing towards the reaction interface due to the confinement effect exerted by the support membrane, the IP reaction tended to generate a leaf/belt-like feature. The reaction continued with the diffusion of additional MPD monomers through the nascent polyamide, and was terminated when it reached self-limiting thickness (20-30 nm) because of the limited diffusivity of the MPD monomers through this rejection film.[60] As a result, the polyamide membrane is formed with an increased effective filtration area as well as a reduced intrinsic thickness, thus improving membrane permeability. At the same time, the impeded heat dissipation by the MOF-loaded support led to an increase of cross-linking degree of PA layer, accounting for the simultaneous improvement of salt rejection rate for the TFC-MOF membranes.

An additional mechanism contributing to the enhancement of water permeance is the reduction of geometric restriction as illustrated in Figure 8. The MOF nanosheets reduced the transport restriction by providing a highly permeable gutter layer, resulting in greatly shortened lateral transport path.[70, 71] Noticeably, the path for water transport through the membranes was totally

different between PES membrane and TFC-MOF membranes. For pristine PES membrane, water was directly flowed into the PES pores without any lateral diffusion. After the coating of MOF nanosheets, the direct path was partially impeded, resulting in reduced permeance. However, for TFC membrane, the porosity of PES support or PES-MOF membrane was not the dominant factor affecting the permeance. Although the MWCO of the PES-MOF decreased, the key barrier of the TFC membrane was polyamide nanofilm. Because of the restriction of polyamide layer, for the pristine TFC membrane, water molecules need to laterally diffuse along the active layer until they reach the surface pores of the support layers since the solid matrix of the support layer (*e.g.*, polyether sulphone in this study) is nearly impermeable.[72] In contrast, for membranes with MOF nanosheet interlayers, the highly porous nanosheets provided channels for water flux into the surface pores of the support layers. This suggested that there was more chance for water flux to diffuse into the surface pores of the support, thereby reducing the geometric restriction and remarkably improving the permeance.[71]

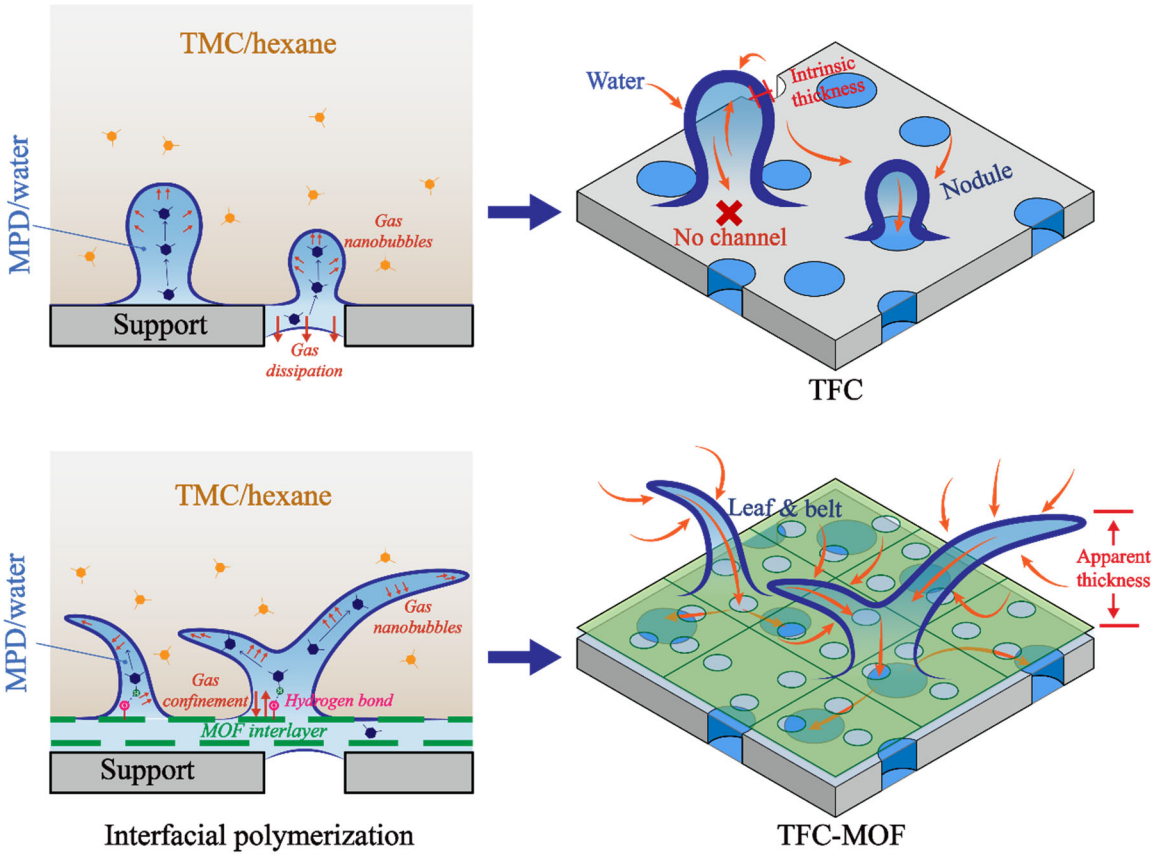

Figure 8. Schematic illustration of the effects of incorporating MOF nanosheets on IP process and PA structure. (a) TFC membrane; (b) TFC-MOF membrane.

CONCLUSIONS

In this study, by incorporating an ultrathin 2D ZnTCPP MOFs interlayer, a novel TFC membrane was developed for water purification. The introduction of 2D MOF nanosheets by filtration provided an ultrathin, compact, and highly ordered laminate interlayer on the PES support. The nanosheets with preferential orientation enabled the formation of a permeable MOF nanosheet layer. Compared to the control, fabricating PA nanofilm on this MOF nanosheet interlayer nearly

tripled the membrane water permeability with a simultaneous increase of NaCl rejection (> 97%), successfully overcoming the permeability-selectivity trade-off. The MOF interlayer induced the significant changes in the polyamide membrane structure that favors water permeation, *i.e.*, decreased intrinsic thickness, increased void volume fraction, and enhanced effective filtration surface area, which is associated with the synergistic effects of enhanced confinement to interfacially degassed nanobubbles and reduced diffusivity of *m*-phenylenediamine monomers. This interlayer also increased the cross-linking degree of polyamide layer, which enhanced the rejection properties of the membranes. Furthermore, by comparing the separation performance between TFC membranes and FR membranes, it could be found that the interlayer also served as a gutter layer to improve the membrane performance.

AUTHOR INFORMATION

Corresponding Author

* Tel.: +86-21-65975669, Fax: +86-21-65980400. E-mail: zwwang@tongji.edu.cn

Notes

The authors declare no competing financial interest.

SUPPORTING INFORMATION

The Supporting Information is available free of charge on the ACS Publications website at DOI:

S1. Characterization of MOF nanosheets; S2. Result and discussion of MOF nanosheets characterization; S3. Zeta potential of PES-MOF-0, PES-MOF-1, PES-MOF-2, and PES-MOF-3 membranes; S4. Cross-section FESEM micrographs of PES and PES-MOF membranes; S5. Measurement of molecular weight cut-off (MWCO) of PES-MOF-0, PES-MOF-1, PES-MOF-2, and PES-MOF-3 membranes; S6. Determination of the apparent and intrinsic thickness of polyamide layers using TEM analysis; S7. Determination of the void volume fraction (*f*) of polyamide layers using TEM analysis; S8. The surface area ratio (SAR) measured by AFM analysis; S9. Variation of mass per unit area and mass uptake of the nanofilms measured with a quartz crystal microbalance; S10. The stability measurement of TFC membranes; S11. Surface and cross-section SEM images of FR-0, FR-1, FR-2, and FR-3 membranes; S12. Measurement of diffusivity of MPD monomers from support membranes; S13. XPS elemental composition of the membranes.

ACKNOWLEDGMENTS

We thank the National Natural Science Foundation of China (Grants 51838009 & 51925806) and Science & Technology Commission of Shanghai Municipality (18DZ1206703) for the financial support of the work.

REFERENCES

(1) Elimelech, M.; Phillip, W.A. The Future of Seawater Desalination: Energy, Technology, and the Environment. *Science* **2011**, 333, 712-717.

(2) Tang, C.Y.; Yang, Z.; Guo, H.; Wen, J.J.; Nghiem, L.D.; Cornelissen, E. Potable Water Reuse through Advanced Membrane Technology. *Environ. Sci. Technol.* **2018**, 52, 10215-10223.

(3) Werber, J.R.; Deshmukh, A.; Elimelech, M. The Critical Need for Increased Selectivity, Not Increased Water Permeability, for Desalination Membranes. *Environ. Sci. Technol. Lett.* **2016**, 3, 112-120.

(4) Koros, W.J.; Zhang, C. Materials for Next-Generation Molecularly Selective Synthetic Membranes. *Nat. Mater.* **2017**, 16, 289-297.

(5) Ma, X.-H.; Yao, Z.-K.; Yang, Z.; Guo, H.; Xu, Z.-L.; Tang, C.Y.; Elimelech, M. Nanofoaming of Polyamide Desalination Membranes to Tune Permeability and Selectivity. *Environ. Sci. Technol. Lett.* **2018**, 5, 123-130.

(6) Yang, Z.; Guo, H.; Yao, Z.-k.; Mei, Y.; Tang, C.Y. Hydrophilic Silver Nanoparticles Induce Selective Nanochannels in Thin Film Nanocomposite Polyamide Membranes. *Environ. Sci. Technol.* **2019**, 53, 5301-5308.

(7) Jiang, Z.; Karan, S.; Livingston, A.G. Water Transport through Ultrathin Polyamide Nanofilms Used for Reverse Osmosis. *Adv. Mater.* **2018**, 30, e1705973.

(8) Kłosowski, M.M.; McGilvery, C.M.; Li, Y.; Abellan, P.; Ramasse, Q.; Cabral, J.T.; Livingston, A.G.; Porter, A.E. Micro-to Nano-Scale Characterisation of Polyamide Structures of the Sw30hr Ro Membrane Using Advanced Electron Microscopy and Stain Tracers. *J. Membr. Sci.* **2016**, 520, 465-476.

(9) Yang, Z.; Guo, H.; Tang, C.Y. The Upper Bound of Thin-Film Composite (Tfc) Polyamide Membranes for Desalination. *J. Membr. Sci.* **2019**, 590, 117297.

(10) Park, H.B.; Kamcev, J.; Robeson, L.M.; Elimelech, M.; Freeman, B.D. Maximizing the Right Stuff: The Trade-Off between Membrane Permeability and Selectivity. *Science* **2017**, 356, eaab0530.

(11) Fridman-Bishop, N.; Freger, V. What Makes Aromatic Polyamide Membranes Superior: New Insights into Ion Transport and Membrane Structure. *J. Membr. Sci.* **2017**, 540, 120-128.

(12) Fujioka, T.; Oshima, N.; Suzuki, R.; Price, W.E.; Nghiem, L.D. Probing the Internal Structure of Reverse Osmosis Membranes by Positron Annihilation Spectroscopy: Gaining More Insight into the Transport of Water and Small Solutes. *J. Membr. Sci.* **2015**, 486, 106-118.

(13) Wong, M.C.Y.; Lin, L.; Coronell, O.; Hoek, E.M.V.; Ramon, G.Z. Impact of Liquid-Filled Voids within the Active Layer on Transport through Thin-Film Composite Membranes. *J. Membr. Sci.* **2016**, 500, 124-135.

(14) Song, X.; Gan, B.; Qi, S.; Guo, H.; Tang, C.Y.; Zhou, Y.; Gao, C. Intrinsic Nanoscale Structure of Thin Film Composite Polyamide Membranes: Connectivity, Defects, and Structure–Property Correlation. *Environ. Sci. Technol.* **2020**, 54, 3559-3569.

(15) Karan, S.; Jiang, Z.; Livingston, A.G. Sub–10 Nm Polyamide Nanofilms with Ultrafast Solvent Transport for Molecular Separation. *Science* **2015**, 348, 1347-1351.

(16) Tan, Z.; Chen, S.; Peng, X.; Zhang, L.; Gao, C. Polyamide Membranes with Nanoscale Turing Structures for Water Purification. *Science* **2018**, 360, 518-521.

(17) Jeong, B.-H.; Hoek, E.M.V.; Yan, Y.; Subramani, A.; Huang, X.; Hurwitz, G.; Ghosh, A.K.; Jawor, A. Interfacial Polymerization of Thin Film Nanocomposites: A New Concept for Reverse Osmosis Membranes. *J. Membr. Sci.* **2007**, 294, 1-7.

(18) Sun, H.; Tang, B.; Wu, P. Development of Hybrid Ultrafiltration Membranes with Improved Water Separation Properties Using Modified Superhydrophilic Metal-Organic Framework Nanoparticles. *ACS Appl. Mater. Interfaces* **2017**, 9, 21473-21484.

(19) Ma, D.; Peh, S.B.; Han, G.; Chen, S.B. Thin-Film Nanocomposite (Tfn) Membranes Incorporated with Super-Hydrophilic Metal-Organic Framework (Mof) Uio-66: Toward Enhancement of Water Flux and Salt Rejection. *ACS Appl. Mater. Interfaces* **2017**, 9, 7523-7534.

(20) Duan, J.; Pan, Y.; Pacheco, F.; Litwiller, E.; Lai, Z.; Pinnau, I. High-Performance Polyamide Thin-Film-Nanocomposite Reverse Osmosis Membranes Containing Hydrophobic Zeolitic Imidazolate Framework-8. *J. Membr. Sci.* **2015**, 476, 303-310.

(21) Wang, Z.; Wang, Z.; Lin, S.; Jin, H.; Gao, S.; Zhu, Y.; Jin, J. Nanoparticle-Templated Nanofiltration Membranes for Ultrahigh Performance Desalination. *Nat. Commun.* **2018**, 9, 2004.

(22) Yang, S.; Zou, Q.; Wang, T.; Zhang, L. Effects of Go and Mof@Go on the Permeation and Antifouling Properties of Cellulose Acetate Ultrafiltration Membrane. *J. Membr. Sci.* **2019**, 569, 48-59.

(23) Peng, Y.; Li, Y.; Ban, Y.; Jin, H.; Jiao, W.; Liu, X.; Yang, W. Metal-Organic Framework Nanosheets as Building Blocks for Molecular Sieving Membranes. *Science* **2014**, 346, 1356-1359.

(24) Lee, J.; Wang, R.; Bae, T.-H. High-Performance Reverse Osmosis Membranes Fabricated on Highly Porous Microstructured Supports. *Desalination* **2018**, 436, 48-55.

(25) Zhu, Y.; Xie, W.; Gao, S.; Zhang, F.; Zhang, W.; Liu, Z.; Jin, J. Single-Walled Carbon Nanotube Film Supported Nanofiltration Membrane with a Nearly 10 Nm Thick Polyamide Selective Layer for High-Flux and High-Rejection Desalination. *Small* **2016**, 12, 5034-5041.

(26) Choi, H.-g.; Shah, A.A.; Nam, S.-E.; Park, Y.-I.; Park, H. Thin-Film Composite Membranes Comprising Ultrathin Hydrophilic Polydopamine Interlayer with Graphene Oxide for Forward Osmosis. *Desalination* **2019**, 449, 41-49.

(27) Yang, Z.; Zhou, Z.W.; Guo, H.; Yao, Z.; Ma, X.H.; Song, X.; Feng, S.P.; Tang, C.Y. Tannic Acid/Fe(3+) Nanoscaffold for Interfacial Polymerization: Toward Enhanced Nanofiltration Performance. *Environ. Sci. Technol.* **2018**, 52, 9341-9349.

(28) Yang, X.; Du, Y.; Zhang, X.; He, A.; Xu, Z.K. Nanofiltration Membrane with a Mussel-Inspired Interlayer for Improved Permeation Performance. *Langmuir* **2017**, 33, 2318-2324.

(29) Wu, M.-B.; Lv, Y.; Yang, H.-C.; Liu, L.-F.; Zhang, X.; Xu, Z.-K. Thin Film Composite Membranes Combining Carbon Nanotube Intermediate Layer and Microfiltration Support for High Nanofiltration Performances. *J. Membr. Sci.* **2016**, 515, 238-244.

(30) Wu, M.; Yuan, J.; Wu, H.; Su, Y.; Yang, H.; You, X.; Zhang, R.; He, X.; Khan, N.A.; Kasher, R.; Jiang, Z. Ultrathin Nanofiltration Membrane with Polydopamine-Covalent Organic Framework Interlayer for Enhanced Permeability and Structural Stability. *J. Membr. Sci.* **2019**, 576, 131-141.

(31) Zhou, Z.; Hu, Y.; Boo, C.; Liu, Z.; Li, J.; Deng, L.; An, X. High-Performance Thin-Film Composite Membrane with an Ultrathin Spray-Coated Carbon Nanotube Interlayer. *Environ. Sci. Technol. Lett.* **2018**, 5, 243-248.

(32) Lin, Y.S.; Kumakiri, I.; Nair, B.N.; Alsyouri, H. Microporous Inorganic Membranes. *Sep. Purif. Methods* **2002**, 31, 229-379.

(33) Zhu, W.; Xiang, G.; Shang, J.; Guo, J.; Motevalli, B.; Durfee, P.; Agola, J.O.; Coker, E.N.; Brinker, C.J. Versatile Surface Functionalization of Metal-Organic Frameworks through Direct

Metal Coordination with a Phenolic Lipid Enables Diverse Applications. *Adv. Funct. Mater.* **2018**, 28, 1705274.

(34) Ma, X.; Yang, Z.; Yao, Z.; Guo, H.; Xu, Z.; Tang, C.Y. Tuning Roughness Features of Thin Film Composite Polyamide Membranes for Simultaneously Enhanced Permeability, Selectivity and Anti-Fouling Performance. *J. Colloid Interface Sci.* **2019**, 540, 382-388.

(35) Song, P.; Natale, G.; Wang, J.; Bond, T.; Hejazi, H.; Siegler, H.d.l.H.; Gates, I.; Lu, Q. 2d and 3d Metal-Organic Framework at the Oil/Water Interface: A Case Study of Copper Benzenedicarboxylate. *Adv. Mater. Interfaces* **2019**, 6, 1801139.

(36) Rodenas, T.; Luz, I.; Prieto, G.; Seoane, B.; Miro, H.; Corma, A.; Kapteijn, F.; Llabres, I.X.F.X.; Gascon, J. Metal-Organic Framework Nanosheets in Polymer Composite Materials for Gas Separation. *Nat. Mater.* **2015**, 14, 48-55.

(37) Zhao, M.; Wang, Y.; Ma, Q.; Huang, Y.; Zhang, X.; Ping, J.; Zhang, Z.; Lu, Q.; Yu, Y.; Xu, H.; Zhao, Y.; Zhang, H. Ultrathin 2d Metal-Organic Framework Nanosheets. *Adv. Mater.* **2015**, 27, 7372-7378.

(38) Park, S.-J.; Choi, W.; Nam, S.-E.; Hong, S.; Lee, J.S.; Lee, J.-H. Fabrication of Polyamide Thin Film Composite Reverse Osmosis Membranes Via Support-Free Interfacial Polymerization. *J. Membr. Sci.* **2017**, 526, 52-59.

(39) Lee, T.H.; Lee, M.Y.; Lee, H.D.; Roh, J.S.; Kim, H.W.; Park, H.B. Highly Porous Carbon Nanotube/Polysulfone Nanocomposite Supports for High-Flux Polyamide Reverse Osmosis Membranes. *J. Membr. Sci.* **2017**, 539, 441-450.

(40) Zhang, X.; Ma, J.; Tang, C.Y.; Wang, Z.; Ng, H.Y.; Wu, Z. Antibiofouling Polyvinylidene Fluoride Membrane Modified by Quaternary Ammonium Compound: Direct Contact-Killing Versus Induced Indirect Contact-Killing. *Environ. Sci. Technol.* **2016**, 50, 5086-5093.

(41) Cheng, Z.L.; Li, X.; Feng, Y.; Wan, C.F.; Chung, T.-S. Tuning Water Content in Polymer Dopes to Boost the Performance of Outer-Selective Thin-Film Composite (Tfc) Hollow Fiber Membranes for Osmotic Power Generation. *J. Membr. Sci.* **2017**, 524, 97-107.

(42) Zhong, P.; Fu, X.; Chung, T.S.; Weber, M.; Maletzko, C. Development of Thin-Film Composite Forward Osmosis Hollow Fiber Membranes Using Direct Sulfonated Polyphenylenesulfone (Sppsu) as Membrane Substrates. *Environ. Sci. Technol.* **2013**, 47, 7430-7436.

(43) Mo, Y.; Tiraferri, A.; Yip, N.Y.; Adout, A.; Huang, X.; Elimelech, M. Improved Antifouling Properties of Polyamide Nanofiltration Membranes by Reducing the Density of Surface Carboxyl Groups. *Environ. Sci. Technol.* **2012**, 46, 13253-13261.

(44) Li, J.; Xiao, L.-T.; Zeng, G.-M.; Huang, G.-H.; Shen, G.-L.; Yu, R.-Q. Amperometric Immunosensor Based on Polypyrrole/Poly(M-Pheylenediamine) Multilayer on Glassy Carbon Electrode for Cytokinin N6-(Δ2-Isopentenyl) Adenosine Assay. *Anal. Biochem.* **2003**, 321, 89-95.

(45) Wen, Y.; Chen, Y.; Wu, Z.; Liu, M.; Wang, Z. Thin-Film Nanocomposite Membranes Incorporated with Water Stable Metal-Organic Framework Cubttri for Mitigating Biofouling. *J. Membr. Sci.* **2019**, 582, 289-297.

(46) Freger, V. Swelling and Morphology of the Skin Layer of Polyamide Composite Membranes: An Atomic Force Microscopy Study. *Environ. Sci. Technol.* **2004**, 38, 3168-3175.

(47) Perry, L.A.; Coronell, O. Reliable, Bench-Top Measurements of Charge Density in the Active Layers of Thin-Film Composite and Nanocomposite Membranes Using Quartz Crystal Microbalance Technology. *J. Membr. Sci.* **2013**, 429, 23-33.

(48) Hu, M.; Zhong, K.; Liang, Y.; Ehrman, S.H.; Mi, B. Effects of Particle Morphology on the Antibiofouling Performance of Silver Embedded Polysulfone Membranes and Rate of Silver Leaching. *Ind. Eng. Chem. Res.* **2017**, 56, 2240-2246.

(49) Wang, J.; Kingsbury, R.S.; Perry, L.A.; Coronell, O. Partitioning of Alkali Metal Salts and Boric Acid from Aqueous Phase into the Polyamide Active Layers of Reverse Osmosis Membranes. *Environ. Sci. Technol.* **2017**, 51, 2295-2303.

(50) Lin, L.; Lopez, R.; Ramon, G.Z.; Coronell, O. Investigating the Void Structure of the Polyamide Active Layers of Thin-Film Composite Membranes. *J. Membr. Sci.* **2016**, 497, 365-376.

(51) Lin, L.; Weigand, T.M.; Farthing, M.W.; Jutaporn, P.; Miller, C.T.; Coronell, O. Relative Importance of Geometrical and Intrinsic Water Transport Properties of Active Layers in the Water Permeability of Polyamide Thin-Film Composite Membranes. *J. Membr. Sci.* **2018**, 564, 935-944.

(52) Lin, L.; Feng, C.; Lopez, R.; Coronell, O. Identifying Facile and Accurate Methods to Measure the Thickness of the Active Layers of Thin-Film Composite Membranes – a Comparison of Seven Characterization Techniques. *J. Membr. Sci.* **2016**, 498, 167-179.

(53) Fujioka, T.; O'Rourke, B.E.; Michishio, K.; Kobayashi, Y.; Oshima, N.; Kodamatani, H.; Shintani, T.; Nghiem, L.D. Transport of Small and Neutral Solutes through Reverse Osmosis Membranes: Role of Skin Layer Conformation of the Polyamide Film. *J. Membr. Sci.* **2018**, 554, 301-308.

(54) Ghosh, A.K.; Hoek, E.M.V. Impacts of Support Membrane Structure and Chemistry on Polyamide–Polysulfone Interfacial Composite Membranes. *J. Membr. Sci.* **2009**, 336, 140-148.

(55) Lu, X.; Arias Chavez, L.H.; Romero-Vargas Castrillon, S.; Ma, J.; Elimelech, M. Influence of Active Layer and Support Layer Surface Structures on Organic Fouling Propensity of Thin-Film Composite Forward Osmosis Membranes. *Environ. Sci. Technol.* **2015**, 49, 1436-1444.

(56) Liu, M.; Xie, K.; Nothling, M.D.; Gurr, P.A.; Tan, S.S.L.; Fu, Q.; Webley, P.A.; Qiao, G.G. Ultrathin Metal-Organic Framework Nanosheets as a Gutter Layer for Flexible Composite Gas Separation Membranes. *ACS Nano* **2018**, 12, 11591-11599.

(57) Peng, L.E.; Yao, Z.; Liu, X.; Deng, B.; Guo, H.; Tang, C.Y. Tailoring Polyamide Rejection Layer with Aqueous Carbonate Chemistry for Enhanced Membrane Separation: Mechanistic Insights, Chemistry-Structure-Property Relationship, and Environmental Implications. *Environ. Sci. Technol.* **2019**, 53, 9764-9770.

(58) Song, X.; Gan, B.; Yang, Z.; Tang, C.Y.; Gao, C. Confined Nanobubbles Shape the Surface Roughness Structures of Thin Film Composite Polyamide Desalination Membranes. *J. Membr. Sci.* **2019**, 582, 342-349.

(59) Ramon, G.Z.; Hoek, E.M.V. Transport through Composite Membranes, Part 2: Impacts of Roughness on Permeability and Fouling. *J. Membr. Sci.* **2013**, 425-426, 141-148.

(60) Yan, H.; Miao, X.; Xu, J.; Pan, G.; Zhang, Y.; Shi, Y.; Guo, M.; Liu, Y. The Porous Structure of the Fully-Aromatic Polyamide Film in Reverse Osmosis Membranes. *J. Membr. Sci.* **2015**, 475, 504-510.

(61) Gong, G.; Wang, P.; Zhou, Z.; Hu, Y. New Insights into the Role of an Interlayer for the Fabrication of Highly Selective and Permeable Thin-Film Composite Nanofiltration Membrane. *ACS Appl. Mater. Interfaces* **2019**, 11, 7349-7356.

(62) Zhang, X.; Lv, Y.; Yang, H.C.; Du, Y.; Xu, Z.K. Polyphenol Coating as an Interlayer for Thin-Film Composite Membranes with Enhanced Nanofiltration Performance. *ACS Appl. Mater. Interfaces* **2016**, 8, 32512-32519.

(63) Wei, J.; Liu, X.; Qiu, C.; Wang, R.; Tang, C.Y. Influence of Monomer Concentrations on the Performance of Polyamide-Based Thin Film Composite Forward Osmosis Membranes. *J. Membr. Sci.* **2011**, 381, 110-117.

(64) Zhang, Z.; Kang, G.; Yu, H.; Jin, Y.; Cao, Y. From Reverse Osmosis to Nanofiltration: Precise Control of the Pore Size and Charge of Polyamide Membranes Via Interfacial Polymerization. *Desalination* **2019**, 466, 16-23.

(65) Yang, Z.; Huang, X.; Ma, X.-h.; Zhou, Z.-w.; Guo, H.; Yao, Z.; Feng, S.-P.; Tang, C.Y. Fabrication of a Novel and Green Thin-Film Composite Membrane Containing Nanovoids for Water Purification. *J. Membr. Sci.* **2019**, 570-571, 314-321.

(66) Shen, L.; Yi, M.; Tian, L.; Wang, F.; Ding, C.; Sun, S.; Lu, A.; Su, L.; Wang, Y. Efficient Surface Ionization and Metallization of Tfc Membranes with Superior Separation Performance, Antifouling and Anti-Bacterial Properties. *J. Membr. Sci.* **2019**, 586, 84-97.

(67) Lau, W.J.; Gray, S.; Matsuura, T.; Emadzadeh, D.; Chen, J.P.; Ismail, A.F. A Review on Polyamide Thin Film Nanocomposite (Tfn) Membranes: History, Applications, Challenges and Approaches. *Water Res.* **2015**, 80, 306-324.

(68) Shi, M.; Wang, Z.; Zhao, S.; Wang, J.; Zhang, P.; Cao, X. A Novel Pathway for High Performance Ro Membrane: Preparing Active Layer with Decreased Thickness and Enhanced Compactness by Incorporating Tannic Acid into the Support. *J. Membr. Sci.* **2018**, 555, 157-168.

(69) Freger, V. Nanoscale Heterogeneity of Polyamide Membranes Formed by Interfacial Polymerization. *Langmuir* **2003**, 19, 4791-4797.

(70) Lee, J.; Yoon, H.; Yoo, J.H.; Choi, D.-C.; Nahm, C.H.; Lee, S.H.; Chae, H.-R.; Kim, Y.H.; Lee, C.-H.; Park, P.-K. Influence of the Sublayer Structure of Thin-Film Composite Reverse Osmosis Membranes on the Overall Water Flux. *Environ. Sci.-Wat. Res. Technol.* **2018**, 4, 1912-1922.

(71) Kattula, M.; Ponnuru, K.; Zhu, L.; Jia, W.; Lin, H.; Furlani, E.P. Designing Ultrathin Film Composite Membranes: The Impact of a Gutter Layer. *Sci. Rep.* **2015**, 5, 15016.

(72) Ramon, G.Z.; Wong, M.C.Y.; Hoek, E.M.V. Transport through Composite Membrane, Part 1: Is There an Optimal Support Membrane? *J. Membr. Sci.* **2012**, 415-416, 298-305.

TOC Art

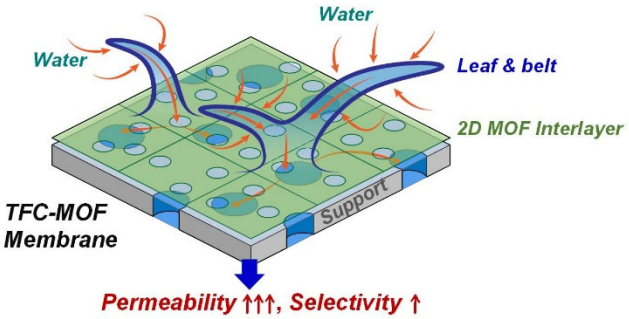
Water
Water
Leaf & belt
2D MOF Interlayer
Support
TFC-MOF
Membrane
Permeability ↑↑↑, Selectivity ↑